RSC Advances

PAPER

Check for updates

Synthesis, structures and properties of six lanthanide complexes based on a 2-(2-carboxyphenyl)imidazo(4,5-*f*)-(1,10) phenanthroline ligand†

Shanshan Ren,[ab] Wei Jiang,[ab] Qingwei Wang,[ab] Zhimin Li,[ab] Yu Qiao [iD] *[ab] and Guangbo Che [iD] *[a]

Six lanthanide complexes [Tb(2-NCP)$_2$(NO$_3$)]$_n$ (**1**), [Eu(2-NCP)$_2$(3-PYC)]$_n$ (**2**), [Sm(2-NCP)$_2$(3-PYC)]$_n$ (**3**), [Eu(2-NCP)(SA)]$_n$ (**4**), [Tb(2-NCP)(SA)]$_n$ (**5**) and [Tb(2-NCP)(AA)]$_n$ (**6**) (2-HNCP = 2-(2-carboxyphenyl) imidazo(4,5-*f*)-(1,10)phenanthroline, 3-HPYC = pyridine-3-carboxylic acid, H$_2$SA = succinic acid, H$_2$AA = adipic acid) have been synthesized by hydrothermal route, and the crystal structures were analyzed through elemental analysis, infrared spectroscopy, single crystal X-ray diffraction. Complexes **1** and **6** present two-dimensional (2D) layers, which are further connected to three-dimensional (3D) supramolecular architectures through C–H⋯π interactions. Complexes **2** and **3** exhibit infinite one-dimensional chains. Finally, the neighboring chains are packed by C–H⋯π interactions, giving rise to 3D supramolecular network. Complexes **4** and **5** display 2D layers, which are further extend to 3D supramolecular structures *via* C–H⋯O intermolecular hydrogen bonding. Six complexes possess good thermal stabilities, characteristic photoluminescence properties, and photocatalytic activities for the degradation of organic dyes under visible light irradiation. In addition, the complex **6** exhibits significantly enhanced photocatalytic activity for methylene blue, and the degradation rate could reach 81.2% in 370 min. Meanwhile trapping experiments indicated that the hole, ·O$_2^-$ and ·OH are the main activated species. Furthermore, by comparing the photoluminescent and photocatalytic mutation results of same metal complexes induced by interconversion of coligands, we confirm that the properties mutation induced by coligands is much obvious and controllable.

Introduction

The past decade has seen an exponential growth of reports dealing with complexes, which are being studied for their possible application in adsorption and separation,[1–4] lumines-cence,[5] magnetism,[6] sensor[7] and catalysis,[8–11] *etc.* Recently, much effort has also been devoted to developing new photo-catalytic materials based on complexes, which is prompted largely by a demand for solving environmental pollution prob-lems owing to their potential applications in the degradation of organic pollutants.[12,13] As an important type of complex with unique structure and characteristic fluorescence *via* lanthanide ions combining with appropriate organic ligands, application of

lanthanide complexes in luminescent materials has received widespread attention.[14–17] Nevertheless, the studies on the photocatalytic properties of lanthanide complexes are relatively rare,[18] therefore, design and synthesis of novel lanthanide complexes with excellent photocatalytic properties have always been the direction of research.

Among the numerous ligands for preparing metal complexes, structural units containing N,O ligands have received extensive attention.[19] 1,10-Phenanthroline derivatives are one of the most unique N,O-containing ligands ascribing to rigid-flexible combining structure. Researchers have also explored phenanthroline derivatives, such as pyrazine(2,3-*f*)-(1,10)phenanthroline,[20] 2-(3-pyridyl)imidazo(4,5-*f*)-(1,10)phe-nanthroline[21,22] 2-(2-carboxyphenyl) imidazo(4,5-*f*)-(1,10)phe-nanthroline (2-HNCP),[23,24] and 2-(4-carboxyphenyl)imidazo(4,5-*f*)-(1,10)phenanthroline[25] and so on. Over the past several years, our group has been dedicated to the syntheses of some carboxyl derivatives of 1,10-phenanthroline to construct complexes and analysis of their luminescence and photocatalysis abilities on organic pollutants.[23–28] It is well known that there is compact relationship between the structures and the properties of

[a]Key Laboratory of Preparation and Application of Environmental Friendly Materials (Jilin Normal University), Ministry of Education, Changchun 130103, P. R. China. E-mail: qiaoyu@jlnu.edu.cn; guangboche@jlnu.edu.cn

[b]College of Chemistry, Jilin Normal University, Siping, 136000, China

complexes, and that the properties of the complexes can be effectively regulated by changing the main ligands and the coligands. Therefore, in order to deeply understand the structure–property relationship of lanthanide complexes based on the carboxyl derivatives of 1,10-phenanthroline, we chose 2-HNCP as the main ligand and pyridine-3-carboxylic acid (3-HPYC), succinic acid (H_2SA), adipic acid (H_2AA) as coligands (Schemes 1 and 2) to construct six complexes: $[Tb(2\text{-}NCP)_2(NO_3)]_n$ (**1**), $[Eu(2\text{-}NCP)_2(3\text{-}PYC)]_n$ (**2**), $[Sm(2\text{-}NCP)_2(3\text{-}PYC)]_n$ (**3**), $[Eu(2\text{-}NCP)(SA)]_n$ (**4**), $[Tb(2\text{-}NCP)(SA)]_n$ (**5**) and $[Tb(2\text{-}NCP)(AA)]_n$ (**6**). In addition, we also conducted a detailed analyses of the thermal stabilities, photoluminescence properties and photocatalytic activities for the degradation of organic dyes of six complexes.

## Experimental section

Characterizing machinery

All of the chemical reagents were obtained Jinan Heng Hua Science and Technology Company and used without further purification. Elemental analysis was performed on a Perkin-Elmer 240 analyzer. The infrared (IR) spectrum was recorded as KBr pellets on a Nicolet iS50 FT-IR Spectrometer in the 4000–400 cm^{-1} region. Powder X-ray diffraction (PXRD) pattern of the complex was collected on a D/MAX-3C diffractometer with the Cu Kα radiation ($\lambda = 1.5406$ Å) at room temperature and 2θ ranging from 5 to 50°. Thermogravimetric analysis (TGA) was performed on a STA 449 F3 Jupiter Synchronous thermal analyzer with a heating rate of 10 °C min^{-1} under air atmosphere. UV-vis diffuse reflectance spectrum (UV-vis DRS) was obtained for the dry-pressed disk samples using a Specord 2450 spectrometer (Shimadzu, Japan) equipped with the integrated sphere accessory for diffuse reflectance spectra, using $BaSO_4$ as the reference reflectance sample. The photoluminescence (PL) spectrum of the complex was obtained by the F4600 (Hitachi, Japan). The photodegradation test was performed by using photocatalytic reactor (DW-01, xenon light source, Yangzhou University teaching instrument factory).

Syntheses of the complexes

Synthesis of complex 1. A mixture of $Tb(NO_3)_3\cdot6H_2O$ (0.0453 g, 0.1 mmol), 2-HNCP (0.0340 g, 0.1 mmol) and 10 mL of H_2O was stirred for 10 min, then the pH value was adjusted to 6.5 by addition of NaOH solution (1 mol L^{-1}). The resultant solution was heated at 443 K in a 25 mL Teflon-lined stainless
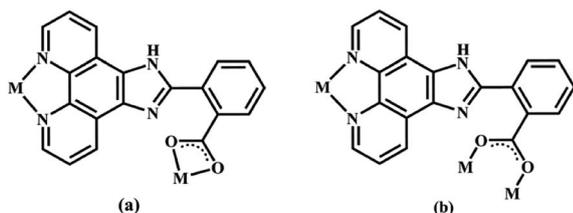
Scheme 1 Two coordination modes of the main ligand 2-NCP⁻ in complexes 1–6 (M = metal).
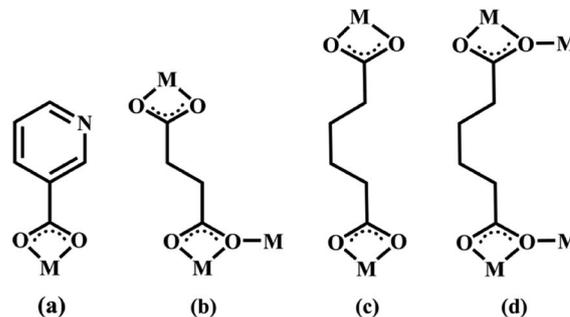
Scheme 2 The coordination modes of 3-PYC⁻, SA²⁻ and AA²⁻ coligands in complexes **2–6** (M = metal).

steel autoclave under autogenous pressure for 3 days. Afterwards, the reaction system was cooled slowly to room temperature. The obtained solid is a mixture of yellow block crystals and powder. The crystals of complex **1** are picked out from the solid mixture in 51% yield based on $Tb(NO_3)_3\cdot6H_2O$. Anal. calc. for $C_{40}H_{22}N_9O_7Tb$ (**1**) (%): C, 53.35; H, 2.44; N, 14.01. Found (%): C, 53.66; H, 2.50; N, 13.98. IR (KBr pellet, cm^{-1}): complex **1**: $\nu =$ 1685 (w), 1615 (m), 1560 (s), 1469 (s), 1421 (s), 1385 (w), 1288 (s), 1184 (m), 1079 (s), 1031 (w), 946 (w), 870 (m), 807 (m), 779 (m), 738 (s), 668 (w), 553 (w), 445 (w). Fig. S1a† exhibits the IR spectrum of the complex **1**.

Synthesis of complex 2. A mixture of $Eu(NO_3)_3\cdot6H_2O$ (0.0446 g, 0.1 mmol), 2-HNCP (0.0680 g, 0.2 mmol), 3-HPYC (0.0123 g, 0.1 mmol) and 10 mL of H_2O was stirred for 10 min, then the pH value was adjusted to 6.5 by addition of NaOH solution (1 mol L^{-1}). The resultant solution was heated at 443 K in a 25 mL Teflon-lined stainless steel autoclave under autogenous pressure for 3 days. Afterwards, the reaction system was cooled slowly to room temperature. The obtained solid is a mixture of yellow block crystals and powder. The crystals of complex **2** are picked out from the solid mixture in 47% yield based on $Eu(NO_3)_3\cdot6H_2O$. Anal. calc. for $C_{46}H_{26}N_9O_6Eu$ (**2**) (%): C, 58.07; H, 2.69; N, 13.31. Found (%): C, 58.00; H, 2.73; N, 13.24. IR (KBr pellet, cm^{-1}): complex **2**: $\nu =$ 1553 (s), 1479 (m), 1414 (s), 1358 (m), 1295 (m), 1184 (w), 1135 (w), 814 (s), 1086 (m), 1041 (w), 953 (w), 866 (m), 814 (s), 779 (w), 731 (s), 692 (w), 640 (w), 479 (w), 445 (w). Fig. S1b† exhibits the IR spectrum of the complex **2**.

Synthesis of complex 3. The synthesis process of complex **3** is very similar to that of **2**, except that the metal salt $Eu(NO_3)_3\cdot6H_2O$ is replaced by $Sm(NO_3)_3\cdot6H_2O$ (0.0444 g, 0.1 mmol), and the crystal color obtained of **3** is yellow. The crystals of complex **3** are picked out from the solid mixture in 59% yield based on $Sm(NO_3)_3\cdot6H_2O$. Anal. calc. for $C_{46}H_{26}N_9O_6Sm$ (**3**) (%): C, 58.03; H, 2.82; N, 13.33. Found (%): C, 58.24; H, 2.93; N, 13.25. IR (KBr pellet, cm^{-1}): complex **3**: $\nu =$ 1591 (s), 1556 (s), 1479 (w), 1414 (s), 1361 (m), 1295 (w), 1191 (w), 1079 (m), 856 (m), 814 (s), 741 (s), 574 (w), 452 (w). Fig. S1c† exhibits the IR spectrum of the complex **3**.

Synthesis of complex 4. A mixture of $Eu(NO_3)_3\cdot6H_2O$ (0.0446 g, 0.1 mmol), 2-HNCP (0.0340 g, 0.1 mmol), H_2SA (0.0108 g, 0.1 mmol) and 10 mL of H_2O was stirred for 10 min,

then the pH value was adjusted to 6.0 by addition of NaOH solution (1 mol L^{-1}). The resultant solution was heated at 453 K in a 25 mL Teflon-lined stainless steel autoclave under autogenous pressure for 3 days. Afterwards, the reaction system was cooled slowly to room temperature. The obtained solid is a mixture of yellow block crystals and powder. The crystals of complex **4** are picked out from the solid mixture in 48% yield based on Eu(NO$_3$)$_3$·6H$_2$O. Anal. calc. for C$_{24}$H$_{15}$N$_4$O$_6$Eu (**4**) (%): C, 45.28; H, 2.57; N, 9.61. Found (%): C, 45.20; H, 2.62; N, 9.67. IR (KBr pellet, cm^{-1}): complex **4**: ν = 3740 (m), 3240 (s), 2925 (m), 1976 (w), 1722 (w), 1607 (w), 1492 (w), 1429 (w), 1076 (s), 929 (s), 806 (s), 737 (w), 659 (s), 475 (m), 451 (s). Fig. S1d† exhibits the IR spectrum of the complex **4**.

Synthesis of complex 5. The synthesis process of complex **5** is very similar to that of **4**, except that the metal salt Eu(NO$_3$)$_3$·6H$_2$O is replaced by Tb(NO$_3$)$_3$·6H$_2$O (0.0453 g, 0.1 mmol). The obtained solid is a mixture of yellow block crystals and powder. The crystals of complex **5** are picked out from the solid mixture in 54% yield based on Tb(NO$_3$)$_3$·6H$_2$O. Anal. calc. for C$_{24}$H$_{15}$N$_4$O$_6$Tb (**5**) (%): C, 46.91; H, 2.44; N, 9.12. Found (%): C, 46.88; H, 2.52; N, 9.20. IR (KBr pellet, cm^{-1}): complex **5**: ν = 3240 (s), 2909 (w), 2339 (w), 1553 (s), 1429 (s), 1068 (m), 937 (m), 814 (s), 775 (s), 667 (s), 483 (w), 459 (w). Fig. S1e† exhibits the IR spectrum of the complex **5**.

Synthesis of complex 6. The synthesis process of complex **6** is very similar to that of **5**, except that H$_2$SA ligand is replaced by H$_2$AA ligand (0.0146 g, 0.1 mmol). The obtained solid is a mixture of yellow block crystals and powder. The crystals of complex **6** are picked out from the solid mixture in 60% yield based on Tb(NO$_3$)$_3$·6H$_2$O. Anal. calc. for C$_{26}$H$_{19}$N$_4$O$_6$Tb (**6**) (%): C, 48.59; H, 2.96; N, 8.72. Found (%): C, 48.53; H, 3.01; N, 8.77. IR (KBr pellet, cm^{-1}): complex **6**: ν = 3228 (m), 2948 (w), 1549 (s), 1435 (m), 1389 (m), 1328 (m), 1079 (m), 820 (s), 744 (s), 653 (w), 516 (w). Fig. S1f† exhibits the IR spectrum of the complex **6**.

X-ray structure determination

Crystal data were collected on Bruker SMART APEX II CCD diffractometer with graphite monochromated Mo-Kα radiation (λ = 0.71073 Å) in the ω scan mode, respectively. All the structures were solved by direct methods using the program SHELXS-2014 (ref. 29) and refined by full-matrix least-squares techniques against F^2 using the SHELXTL-2014 (ref. 30) crystallographic software package. All of the non-hydrogen atoms were easily found from the different Fourier map and refined anisotropically, whereas the hydrogen atoms of the complexes were placed by geometrical considerations and were added to the structure factor calculation. The crystallographic data of six complexes are summarized in Table S1† and the selected bond distances and angles in Table S2.†

Results and discussion

Structural analysis of complexes

Structure of [Tb(2-NCP)$_2$(NO$_3$)]$_n$ (1). Complex **1** crystallizes in the monoclinic space group $P2_1/n$. The asymmetric unit consists of one independent Tb^{3+} cation, two 2-NCP$^-$ anions, and one

NO$_3^-$ anion. As shown in Fig. 1, Tb^{3+} cation is ten-coordinated and encircled by four nitrogen atoms (N1, N2, N5, N6) from two chelating 2-NCP$^-$ ligands, and six oxygen atoms (O1$^{#2}$, O2$^{#2}$, O3$^{#1}$, O4$^{#1}$, O5, O6, symmetry codes: #1: $-x$, $-y$ + 1, $-z$ + 2; #2: x $-$ 1/2, $-y$ + 1/2, z $-$ 1/2) from other two different 2-NCP$^-$ ligands and one NO$_3^-$. The Tb–N and Tb–O lengths lie in the range of 2.539(3)–2.646(3) Å and 2.441(3)–2.590(3) Å, respectively, which are in accordance with the previous reports.[31–35] Each 2-NCP$^-$ ligand coordinates with two Tb^{3+} cations in bidentate fashion. In 2-NCP$^-$ ligand, the nitrogen atoms of pyridyl ring chelate one Tb^{3+} cation and the carboxylate group adopts μ^1-η^1:η^1 coordination mode to link one Tb^{3+} ion (Scheme 1a). The adjacent Tb(NO$_3$)$^{2+}$ cations are held by a couple of antiparallel 2-NCP$^-$ ligands to form a [Tb$_2$(2-NCP)$_2$(NO$_3$)$_2$] dimeric unit where the Tb–Tb distance is 9.63 Å. Furthermore, the dimeric units are gathered through independent 2-NCP$^-$ linkers to form an infinite two-dimensional (2D) layer (Fig. 2). Among the layers, there exist edge-to-face C–H···π interactions between C8 and the phenyl rings of 2-NCP$^-$ anions (d(C8–H8···π) = 3.591 Å, <(C8–H8···π) = 103°), which lead to a three-dimensional (3D) supramolecular architecture (Fig. 3).

Structures of [Eu(2-NCP)$_2$(3-PYC)]$_n$ (2) and [Sm(2-NCP)$_2$(3-PYC)]$_n$ (3). Single-crystal X-ray analyses reveal that complexes **2** and **3** are isostructural and differ only in different lanthanide metal centers. Herein, the crystal structure of complex **2** is discussed as a representative. Complex **2** crystallizes in the space group $P\bar{1}$. In the asymmetric unit, there are one crystallographically unique Eu^{3+} ion, two unique 2-NCP$^-$ anions and one 3-PYC$^-$ ligand. As depicted in Fig. 4, the Eu^{3+} ion is in a ten-coordinated environment, completed by six oxygen atoms (O1$^{#1}$, O2$^{#1}$, O3$^{#2}$, O4$^{#2}$, O5, O6, symmetry codes: #1: $-x$ + 2, $-y$, $-z$ + 2; #2: $-x$ + 1, $-y$ + 1, $-z$ + 1) from two independent 2-NCP$^-$ anions and one terminal 3-PYC$^-$ ligand, and four nitrogen atom (N1, N2, N5, N6) from two 2-NCP$^-$ anions. The Eu–N and Eu–O lengths are in the range of 2.569(3)–2.689(3) Å and 2.421(3)–2.664(3) Å, respectively. The distances are comparable to those in the reported Eu^{3+} complexes.[27,28,34–36] Notably, every pair of
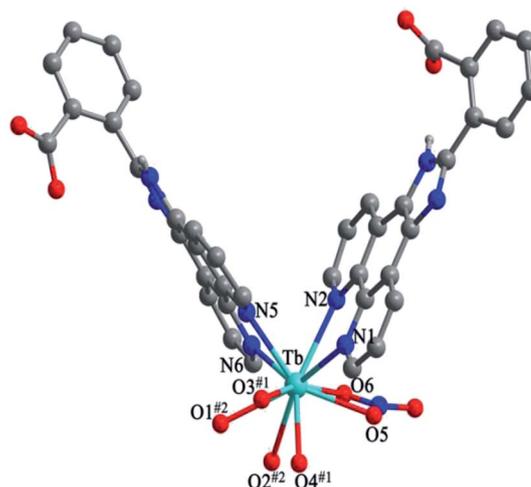

Fig. 1 View of the coordination environment around Tb^{3+} in **1**. Symmetric codes: #1: $-x$, $-y$ + 1, $-z$ + 2; #2: x $-$ 1/2, $-y$ + 1/2, z $-$ 1/2.
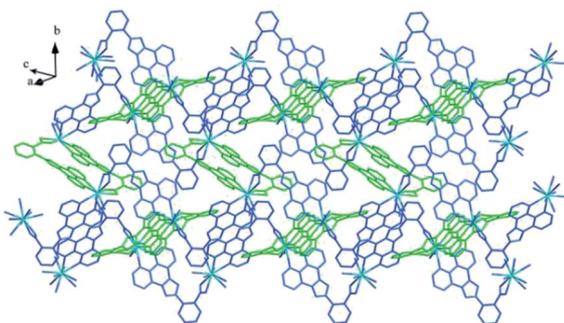
Fig. 2 View of the 2D layer of **1**.

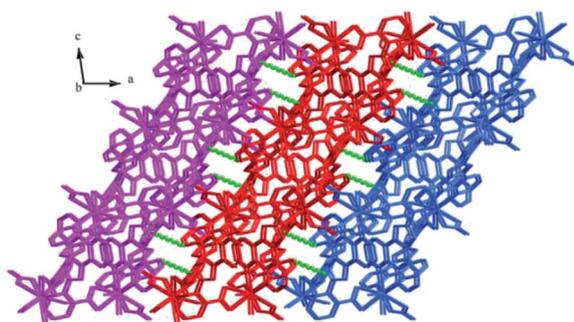Fig. 3 The 3D supramolecular architecture of **1** connected by C–H··· π interactions.
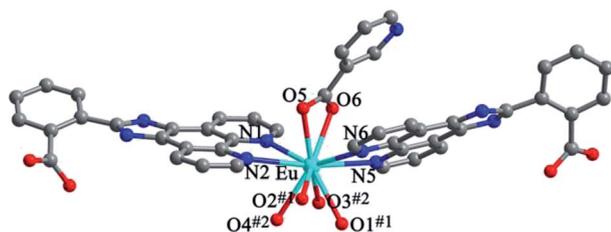

Fig. 4 View of the coordination environment of Eu^{3+} in **2**. Symmetry codes: #1: $-x + 2$, $-y$, $-z + 2$; #2: $-x + 1$, $-y + 1$, $-z + 1$.

antiparallel 2-NCP$^-$ anions connects neighboring Eu(2-PYC)$^{2+}$ cations to give a [Eu$_2$(2-NCP)$_2$(2-PYC)$_2$] dimeric unit (the coordination modes of two ligands shown in Schemes 1a and 2a). With Eu^{3+} ions lying on the inversion center, the adjoining dimeric units are held together to give an infinite 1D chain (Fig. 5). In addition, the chains are sequentially joined by C–H··· π interactions between C16 and the phenyl rings of 2-NCP$^-$
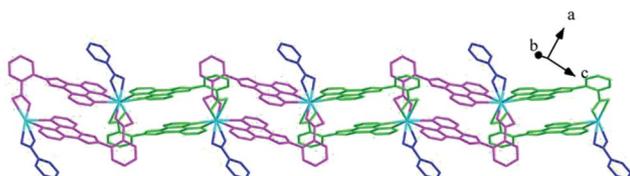

Fig. 5 View of the 1D chain of **2**.

anions (d(C16–H16···π) = 3.373 Å, <(C16–H16···π) = 105°) to generate a 2D framework (Fig. 6). Also, edge-to-face C–H···π interactions are observed between the carbon atoms on 3-PYC$^-$ anions and the phenyl rings of 2-NCP$^-$ anions (d(C44–H44···π) = 3.697 Å, <(C16–H16···π) = 136°), which join the 2D layers to a 3D supramolecular architecture (Fig. 7).

Structures of [Eu(2-NCP)(SA)]$_n$ (4) and [Tb(2-NCP)(SA)]$_n$ (5). In complexes **4** and **5**, the auxiliary ligands have been changed from monocarboxylic ligands to dicarboxylic H$_2$SA, which result in legible "pillar-chain" type 2D layers. Complexes **4** and **5** are isomorphous and display similar 3D supramolecular frameworks. Therefore, only the description of **4** is given in detail. Single crystal X-ray diffraction reveals that complex **4** belongs to the triclinic system and its space group is $P\bar{1}$. The asymmetric unit contains one crystallographically independent Eu^{3+} ion, one 2-NCP$^-$ ligand, and one SA^{2-} anion. As shown in Fig. 8, Eu^{3+} ion is in a nine-coordinated mode, and encircled by two nitrogen atoms (N1$^{\#4}$, N2$^{\#4}$, symmetry codes: #4: $-x + 2$, $-y + 1$, $-z + 1$) from one 2-NCP$^-$ ligand and seven oxygen atoms (O1, O2$^{\#1}$, O3, O4, O5$^{\#3}$, O6$^{\#2}$, O6$^{\#3}$, symmetry codes: #1: $-x + 2$, $-y + 1$, $-z + 2$; #2: $-x + 3$, $-y + 1$, $-z + 2$; #3: $x - 1$, y, z) from two 2-NCP$^-$ anions and three SA^{2-} anions, respectively. The Eu–O and Eu–N lengths distances in **4** are in the range of 2.382(6)–2.610(6) Å and 2.539(7)–2.572(7) Å, respectively, which are in accordance with previous reports.[27,28,34–36] Adjoining Eu^{3+} ions are held together by four carboxylate groups to afford a paddle wheel-like [Eu$_2$] cluster with the Eu–Eu separation of 3.85 Å. Two antiparallel 2-NCP$^-$ ligands bridge the adjacent clusters in trident coordination mode to form a dimeric unit (the coordination mode of 2-NCP$^-$ shown in Scheme 1b). With the [Eu$_2$] cluster as the symmetric center, adjacent dimer units are held together to generate an infinite 1D chain. Moreover, the SA^{2-} anions adopt μ^3-η^2:η^1:η^1:η^1 coordination modes (Scheme 2b) and pillar the neighboring chains to give a "pillar-chain" type 2D layer (Fig. 9). Additionally, there are C–H···O intermolecular hydrogen-bonding interactions between carbon atoms and carboxylate oxygen atoms (d(C8–H8···O4$^{\#5}$) = 3.189 Å, <(C8–H8···O4$^{\#5}$) = 136°, symmetry code: #5: $-x + 2$, $-y$, $-z + 1$), which extend the 2D layers to a 3D framework (Fig. 10).

Structure of [Tb(2-NCP)(AA)]$_n$ (6). In complex **6**, H$_2$SA ligand has been replaced by H$_2$AA with more flexible and longer nature. Single-crystal X-ray analysis reveals that complex **6** also
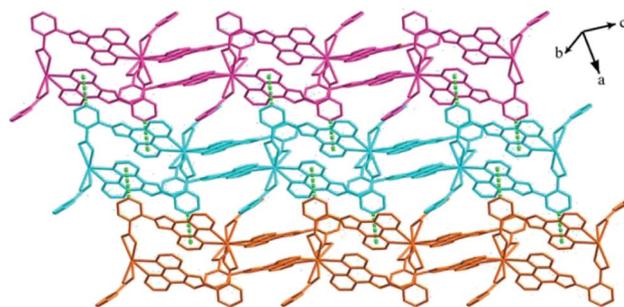

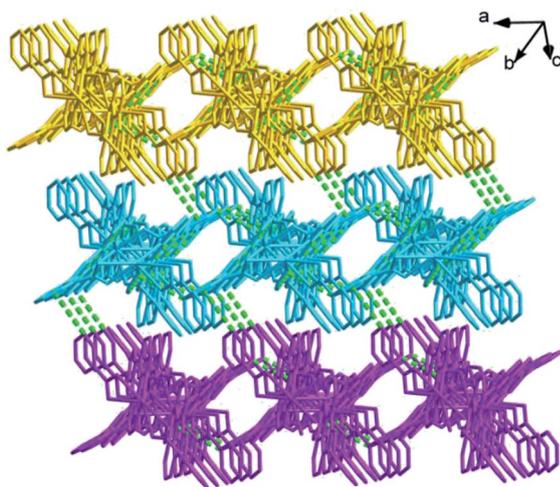Fig. 6 View of the 2D supramolecular layer of **2** stabilized by C−H···π interactions.

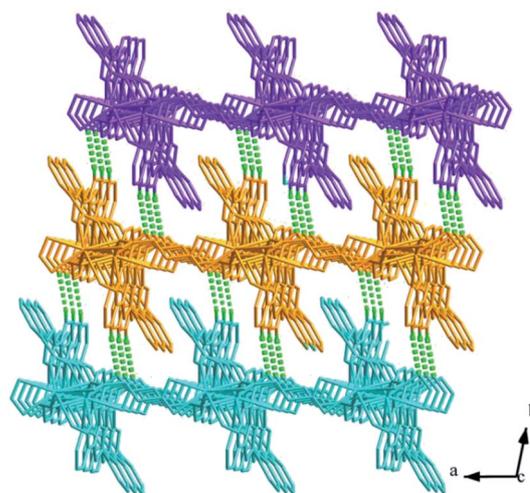Fig. 7 View of the 3D supramolecular architecture of **2** formed by C–H···π interactions.

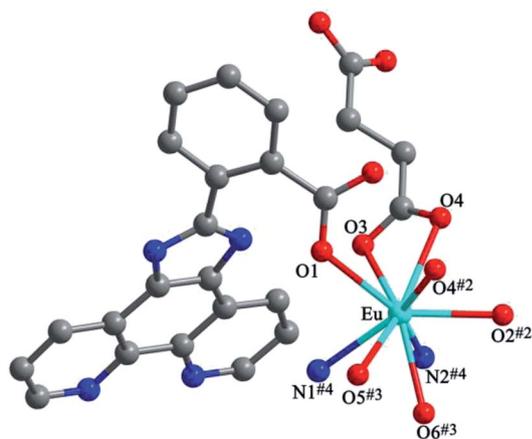Fig. 10 View of the 3D supramolecular architecture of **4** formed by C–H···O interactions.

Fig. 8 View of the coordination environment of Eu^{3+} in **4**. Symmetry codes: #2: −x + 2, −y + 2, −z + 2; #3: x + 1, y, z; #4: −x + 2, −y + 2, −z + 1.
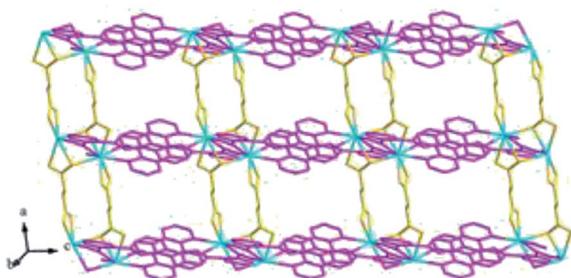

Fig. 9 View of the "pillar–chain" type 2D layer in **4**.

NCP$^-$ ligand bridges three Tb^{3+} ions in a trident coordination fashion and adjacent Tb^{3+} ions are held by carboxylate groups to form a [Tb$_2$] cluster (Scheme 1b). It should be pointed out that the coordination environments of metal ion and 2-NCP$^-$ ligand in **6** are similar with those in complex **4**, which inevitably results in an analogous 1D chain. Then the chains are pillared by AA^{2-} ligands to afford a 2D layer. However, in comparison with complex **4**, the neighboring "pillars" AA^{2-} ligands adopt μ^2-η^1:η^1:η^1:η^1 and μ^4-η^2:η^1:η^2:η^1 coordination modes (Schemes 2c and d), respectively, and exhibit unparallel fashion, which leads to an oblique "pillar-chain" type 2D layer (Fig. 12). In addition, intermolecular C–H···π interactions are observed between carbon atoms and phenyl rings of 2-NCP$^-$ anions (d(C17–H17···π) = 3.982 Å, <(C17–H17···π) = 83°). The 2D layers are further extended by these intermolecular interactions to generate a 3D supramolecular framework (Fig. 13).

Influence of coligands

Complexes **1–6** were synthesized under similar conditions by using identical 2-HNCP main ligands and lanthanide metal salts. From the structure description above, their diverse motifs can be ascribed to the difference of coligands. In complexes **1–6**, coligands have different steric hindrance, flexibility and

exhibits "pillar-chain" type 2D layer. The asymmetric unit contains one independent Tb^{3+} ion, one 2-NCP$^-$ ligand and two half AA^{2-} anions (Fig. 11). Tb^{3+} ion is nine-coordinated and surrounded by three 2-NCP$^-$ ligands and three AA^{2-} anions. The average Tb–O (2.418(2) Å) and Tb–N (2.538(3) Å) distances for **6** are close to those of reported Tb^{3+} complexes.[31–35] Each 2-
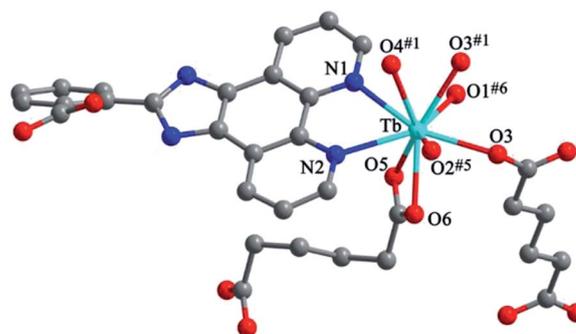

Fig. 11 View of the coordination environment of Tb^{3+} in **6**. Symmetry code: #1: −x + 2, −y, −z + 2; #5: −x + 2, −y, −z + 1; #6: x, y, z + 1.
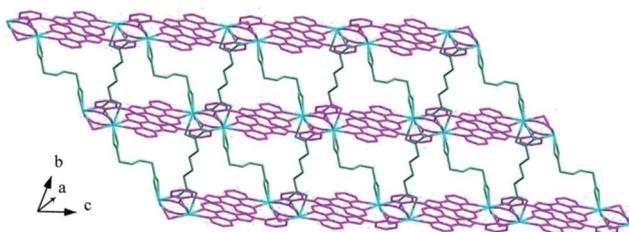
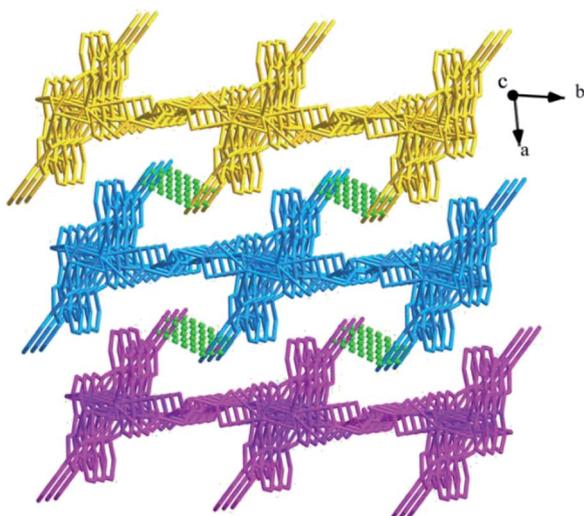Fig. 12   View of the oblique "pillar-chain" type 2D layer in 6.

Fig. 13   View of the 3D supramolecular architecture of 6 furnished via C−H⋯π interactions.

number of carboxylate group. These factors influence the structure of the complexes. Complexes **1** and **2** exhibit the effects of steric hindrance on their structures. In complex **2**, the rigid 3-PYC$^-$ anions hinder the expansion of structure dimension, yielding a 1D chain. Complexes **4–6** imply the number of carboxylate group influence on the structure motifs. Compared with nitrite ion and 3-HPYC, H$_2$SA and H$_2$AA have additional carboxylate group. Generally, extra carboxylate group can increase the coordination patterns of ligands. In complexes **4–6**, SA^{2-} and AA^{2-} anions gather the metal clusters and then support the adjacent chains. While in complexes **1–3**, nitrite ions and 3-PYC$^-$ anions only act as terminal ligands. Additionally, the flexibility of ligands equally affects the complexity of structures. In comparison with SA^{2-} in **4**, AA^{2-} has four −(CH$_2$)− spacers and exhibits more flexible, indicating more unpredictable coordination mode of AA^{2-} anions. As a result, AA^{2-} anions adopt two kinds of coordination patterns in complex **6** and do not pillar the chains parallelly, which lead to an oblique "pillar-chain" type 2D layer.

PXRD and TGA

In order to ensure that the crystal powder is pure phase, the purity of the bulk materials of the complexes **1–6** were tested by PXRD (Fig. 14). The results show that the test values of the samples were consistent with those simulated from the single

crystal X-ray diffraction data except for the relative intensity variation because of preferred orientation of the crystal, indicating that the samples have high purity. As depicted in Fig. 15, one obvious weight loss of 81.4%, 83.2%, 85.0%, 74.6%, 74.7% and 75.0% in the temperature range of 386–769, 394–732, 402–729, 215–556, 223–537 and 386–817 °C are assigned to the decomposition of framework for **1–6** (calcd: 82.3%, 84.0%, 84.2%, 75.0%, 74.1% and 75.3%), respectively. The final residue of 18.6%, 16.8%, 15%, 25.4%, 25.3%, 25% could correspond to the formation of metal oxide (calcd: Tb$_4$O$_7$, 20.7%, **1**; Eu$_2$O$_3$, 18.4%, **2**; Sm$_2$O$_3$, 18.3%, **3**; Eu$_2$O$_3$, 28.9%, **4**; Tb$_4$O$_7$, 30.4%, **5**; Tb$_4$O$_7$, 29.1%, **6**). The thermal analyses products were identified by PXRD (Fig. S2,† JCPDS no. 32-1286, 34-0392 and 42-1461).

Photoluminescent properties

It is well known that ligand-sensitized lanthanide(III) complexes usually possess characteristic photoluminescence properties.[14–17,37,38] Hence the solid-state fluorescence spectra of complexes **1–6** are investigated. The emission spectra of **1**, **5** and **6** at room temperature are shown in Fig. 16, and are typical for the visible emission bands of Tb-based complexes related to literatures. Upon excitation (λ_{ex} = 365 nm, 365 nm, 372 nm, respectively), four characteristic peaks of Tb^{3+} are observed, which correspond to the characteristic emission of $^5D_4 \rightarrow {}^7F_6$, $^5D_4 \rightarrow {}^7F_5$, $^5D_4 \rightarrow {}^7F_4$ and $^5D_4 \rightarrow {}^7F_3$ (491 nm, 546 nm, 591 nm
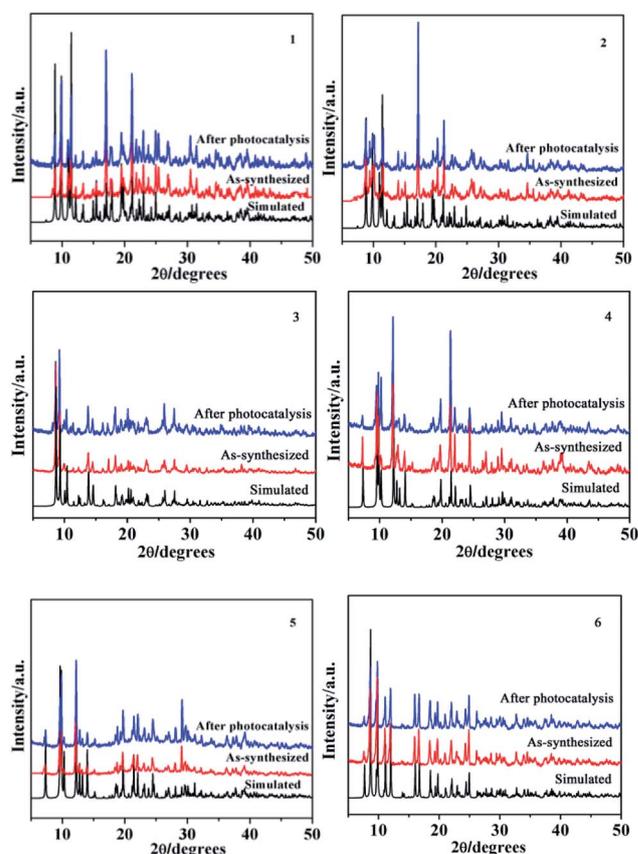

Fig. 14   Simulated, as-synthesized and after photocatalysis powder XRD patterns of **1–6**.
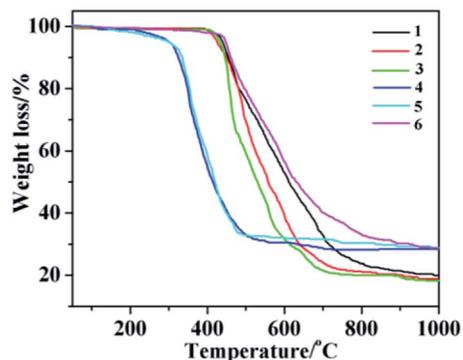
Fig. 15   TG curves of **1–6**.

and 618 nm for **1**; 492 nm, 546 nm, 593 nm, 618 nm for **5**; 492 nm, 546 nm, 586 nm, 621 nm for **6**), respectively.[39] Among of them, the intensity of the characteristic peak with a wavelength of about 618 nm of **1**, 618 nm of **5** and 546 nm of **6** are the strongest. Upon excitation band at 417 nm and 365 nm, respectively, complexes **2** and **4** produced characteristic bands
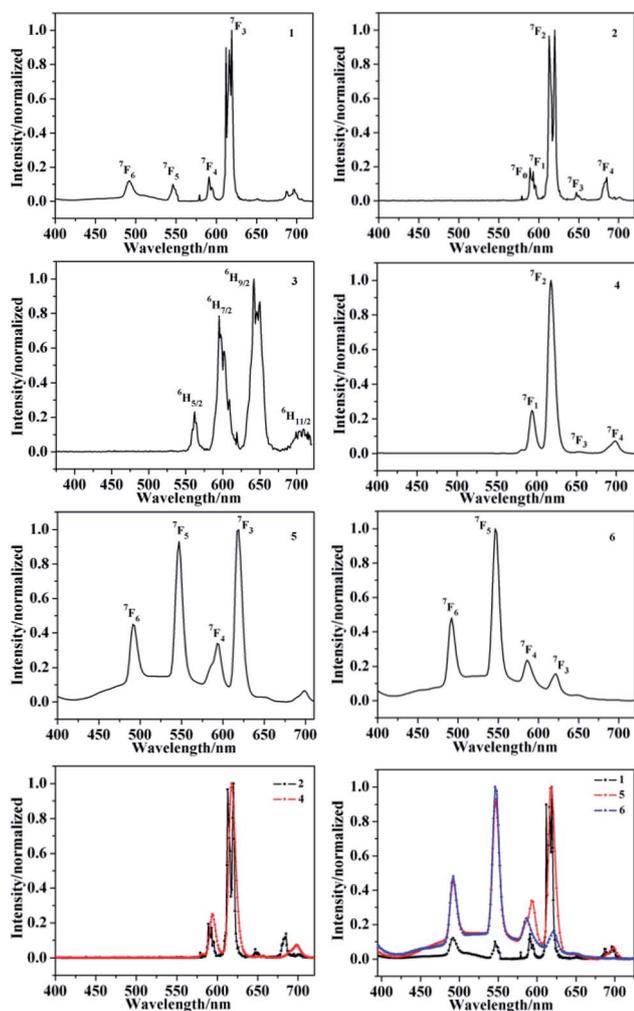
of Eu^{3+} in the visible region, peaking at 592 nm, 613 nm, 646 nm, 684 nm for **2** and 593 nm, 618 nm, 653 nm, 698 nm for **4** which are responsible for the transitions from the emitting $^5D_0 \rightarrow {}^7F_1$, $^5D_0 \rightarrow {}^7F_2$, $^5D_0 \rightarrow {}^7F_3$ and $^5D_0 \rightarrow {}^7F_4$.[39] The strongest peak positions of two europium complexes appear at 613 nm and 618 nm, respectively. It is worthy to note that the difference of the emissive intensity, the strongest peak and peak splitting of Tb^{3+} or Eu^{3+} complexes can be attributed to the different energy levels of different coligands in the three complexes, so the efficiency of energy transfer is different, manifested in intensity and peak position. After excitation at 371 nm, the emission spectrum of complex **3** exhibits the characteristic luminescence bands of Sm^{3+} ions. Complex **3** displays four characteristic bands peaking at 562 nm, 594 nm, 642 nm and 709 nm ascribed to the $^4G_{5/2} \rightarrow {}^6H_{5/2}$, $^4G_{5/2} \rightarrow {}^6H_{7/2}$, $^4G_{5/2} \rightarrow {}^6H_{9/2}$ and $^4G_{5/2} \rightarrow {}^6H_{11/2}$, respectively.[39]

UV-vis diffuse reflectance spectrum

UV-visible diffuse reflectance spectroscopy is commonly used to study the light absorption and energy band characteristics of semiconductors. As shown in Fig. 17a, it is a solid UV-vis diffuse-reflectance spectra of complexes **1–6** and ligands 2-HNCP, 3-Hpyc, H_2SA and H_2AA. The UV-vis DRS of complexes **1–6** and ligand 2-HNCP almost overlaps, and the edge of the absorption band is located at 550 nm. This shows that the absorption of complexes **1–6** depends on the property of ligand 2-HNCP, and can respond in the visible light region, effective use of Xe lamp to degrade organic pollutants. In addition, in

Fig. 16   PL spectra of complexes **1–6**.
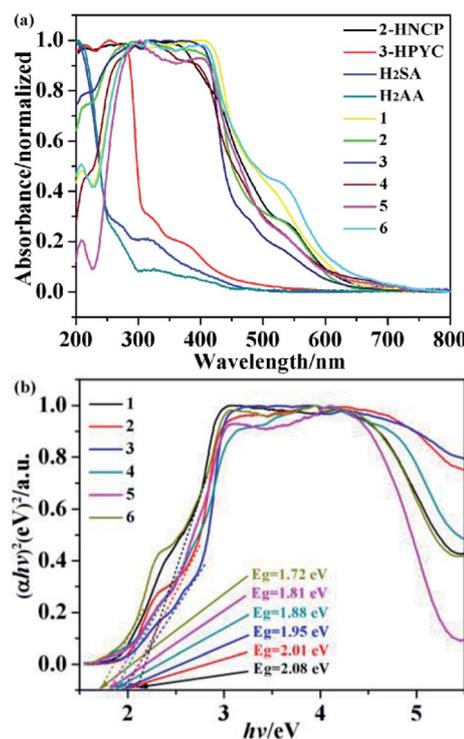

Fig. 17   (a) UV-vis diffuse-reflectance spectra of the complexes **1–6**, 2-HNCP, 3-HPYC, H_2SA and H_2AA ligands with $BaSO_4$ as background; (b) the plots of $(\alpha h\nu)^2$ versus $(h\nu)$ of the complexes **1–6**.

order to explore the conductivity of the title complexes, the measurement of diffuse reflectivity for a powder sample was used to obtain its band gap E_g, the band gap energy (E_g) of the complexes were calculated by the following formula based on the DRS result (1):

$$\alpha h v = A(h v - E_g)^{n/2} \qquad (1)$$

where α is the absorption coefficient, n is the optical frequency, E_g is the band gap energy, A is a constant, respectively. Among of them, the value of n is determined by the type of optical transition of the semiconductor (i.e., $n = 1$ for direct transition and $n = 4$ for indirect transition). According to previous literature reports,[40] for complexes **1–6** as a direct transition, the value of n is 1. Thus, as shown in Fig. 17b, the E_g of the complexes **1–6** are 2.08 eV, 2.01 eV, 1.95 eV, 1.88 eV, 1.81 eV and 1.72 eV, respectively.

Photocatalytic studies

Prior research showed that some lanthanide(III) complexes have attracted attention due to their potential application fields, these are promising photocatalysts for the purifying water and air by completely decomposing organic pollutants.[18] As part of the study to evaluate the efficiency of these six complexes as possible photocatalysts, we selected methylene blue (MB) as a model pollutant for degradation experiments. Typically, a suspension containing **1–6** (30 mg) and 100 mL MB (0.5 mg L^{-1}) solution was stirred in the dark for about 40 minutes. Then turn on the Xe lamp source and remove the clear solution every 30 minutes. The characteristic absorption of MB (approximately 664 nm) was selected to monitor the photocatalytic degradation process. The reflectance spectra show that there exist the optical band gap and semiconductive behaviors in complexes. So these complexes can be employed as potential semiconductive materials. In addition, the concentrations of MB versus reaction time in the presence of complexes **1–6** are shown in Fig. 18a. The degradation efficiencies are defined as C/C_0, where C and C_0 represent the remnant and initial concentration of MB, respectively. After the irradiation time of 370 min, the MB degradation rates were 5.0%, 19.6%, 20.5%, 24.6%, 37.8%, 41.4% and 81.2% without and with **1–6** as photocatalysts, respectively. The results revealed that the order of the catalytic activities of six complexes was **6 > 5 > 4 > 3 > 2 > 1**. These results suggest that the complex **6** may be a good candidate for the photocatalytic degradation of MB.

In order to describe the rate of degradation reaction for these samples, the corresponding reaction rate constant (k) was calculated by adopting the pseudo-first-order kinetic equation according to the Langmuir–Hinshelwood model. At the same time, the kinetic behaviors of photocatalytic degradation using the composite photocatalysts were further investigated, and the results are shown in Fig. 18b. All of them fit well with the pseudo-first-order correlation: $\ln(C_0/C) = kt$, where C is the concentration of organic dye remaining in the solution at an irradiation time of t, C_0 is the initial concentration at $t = 0$, and k is the degradation apparent rate constant (min^{-1}). It is found that the k values were calculated to be 5.13×10^{-4} min^{-1} for **1**,
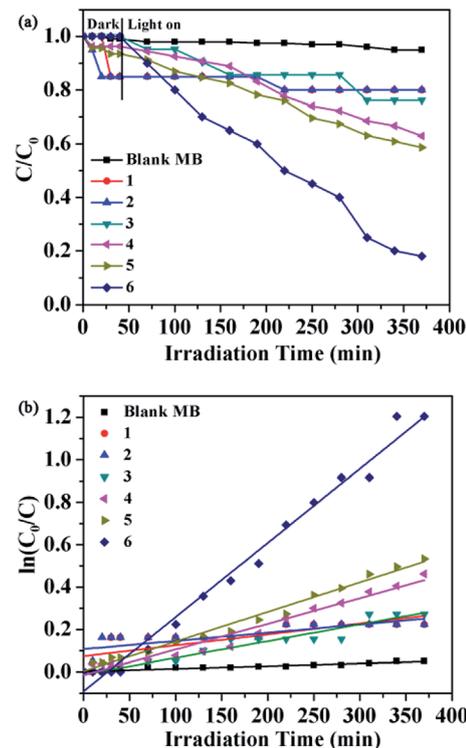

Fig. 18 (a) The photocatalytic activities of complexes **1–6** for MB of degradation under visible light; (b) the pseudo-first-order plot for the photodegradation of MB in the presence of **1–6** under visible light irradiation. The dots and line represent the experimental data and the fitted least-square line, respectively.

3.87×10^{-4} min^{-1} for **2**, 7.88×10^{-4} min^{-1} for **3**, 1.21×10^{-3} min^{-1} for **4**, 1.4×10^{-3} min^{-1} for **5**, 3.5×10^{-3} min^{-1} for **6** and 1.24×10^{-4} min^{-1} for the blank experiment. The dots of the experimental data and the fitted least-square line show the $R^2 = 0.5970$ for **1**, $R^2 = 0.5617$ for **2**, $R^2 = 0.9393$ for **3**, $R^2 = 0.9636$ for **4**, $R^2 = 0.9853$ for **5**, $R^2 = 0.9848$ for **6** and $R^2 = 0.9166$ for the blank. In comparison with the calculated results, the effect of photocatalyst addition was a significant speed up of the discoloration processes. In addition, the stabilities of **1–6** were monitored using PXRD during the photocatalytic process. After photocatalysis, six complexes display similar PXRD patterns to the original (Fig. 14), implying that the stabilities toward photocatalytic reactions for **1–6** are excellent.

Herein, four organic dyes RhB, MO, MV and CR were selected as model pollutants in aqueous media to evaluate the photocatalytic effectiveness of complex **6**. It can be seen that approximately 55% of RhB, 25% of MO, 44% of MV and 40% of CR have been decomposed after 370 min of irradiation for **6**, respectively (Fig. 19a). These results indicated that the complex **6** is more active for the decomposition of RhB under visible light irradiation. This is good candidates for photocatalytic degradation of RhB. All of them fit well with the pseudo-first-order correlation: $\ln(C_0/C) = kt$. The order of different organic dyes degradation rate for as-prepared photocatalyst **6** was RhB (1.89×10^{-3} min^{-1}) > MV (1.42×10^{-3} min^{-1}) > CR (1.12×10^{-3} min^{-1}) > MO (8.54×10^{-4} min^{-1}) > blank ($1.26 \times$
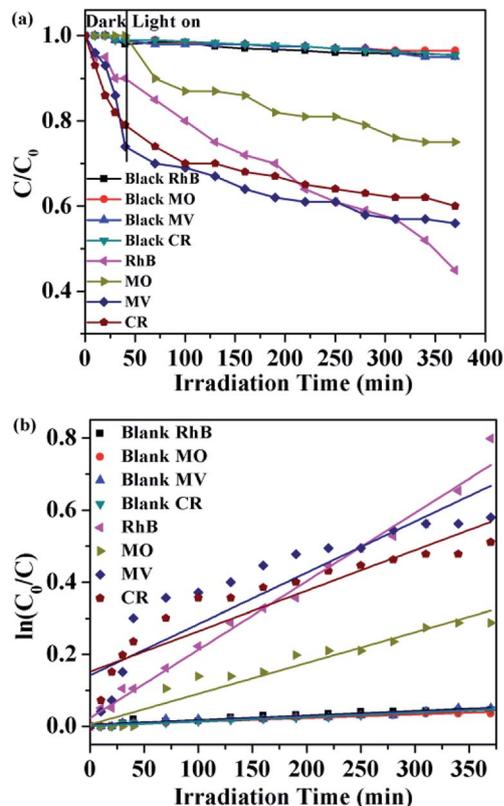
Fig. 19 (a) The photocatalytic activities of **6** for different organic dyes of degradation under visible light; (b) the first-kinetic of the photocatalytic degradation of four organic dyes. The dots and line represent the experimental data and the fitted least-square line, respectively.

10^{-4} min^{-1}, 1.24×10^{-4} min^{-1}, 1.21×10^{-4} min^{-1}, 1.00×10^{-4} min^{-1}, respectively) (Fig. 19b). The dots of the experimental data and the fitted least-square line show the $R^2 = 0.9859$ for RhB, $R^2 = 0.9391$ for MO, $R^2 = 0.8075$ for MV, $R^2 = 0.8142$ for CR and $R^2 = 0.9059$ for the blank RhB, $R^2 = 0.9406$ for the blank MO, $R^2 = 0.9166$ for the blank MV, $R^2 = 0.9774$ for the blank CR. In comparison with the calculated results, the effect of photocatalyst addition also was a significant speed up of the discoloration processes.

Photocatalytic mechanism

The mechanism of the photodegradation of organic pollutant catalyzed by complexes was illustrated as follows: the electrons of these complexes could be excited electrons (e^-) from the valence band (VB) to the conduction band (CB) under the irradiation of visible light, generating the same amount of holes (h^+). The key intermediate, hydroxyl radical ($\cdot OH$), was yielded by the combination of H^+ with $\cdot O_2^-$ generated from the reduction of O_2 by e^- and the oxidation of OH^- oxidized by h^+. The $\cdot OH$ radical was so active as to decompose the organic pollutants into other products, CO_2, and H_2O.[41,42] Based on the above results, the complex **6** has good photocatalytic activity for MB. In order to clarify the photocatalytic mechanism of MB, trapping experiments of radicals were used to detect the main oxidative species in the photocatalytic process.[23,43,44]
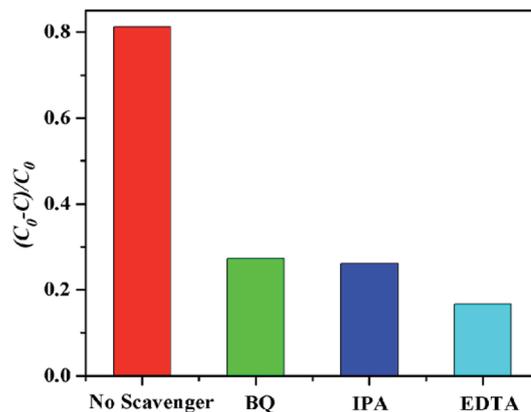

Fig. 20 Plots of radical trapping in the system of photodegradation of MB by complex **6** under visible light irradiation.

Taking the photodegradation of MB as an example, the degradation rate of complex **6** under visible light without the addition of scavenger can reach 81.2%, respectively. As shown in Fig. 20 for the as-prepared sample, it can be seen that when the radical scavenger EDTA (as a hole scavenger) was added into reaction solution, the degradation rate of MB obviously was inhibited (16.67% for **6**). At the same time, when the radical scavenger isopropyl alcohol (IPA, as a $\cdot OH$ scavenger) and p-benzoquinone (BQ, as a $\cdot O_2^-$ scavenger) were added into reaction solution, the degradation rate of MB was inhibited (26.09% and 27.27% for **6**). Therefore, combined with the above discussion, the possible photocatalytic mechanism for degradation of MB with the photocatalyst **6** was proposed as shown in Fig. 21. On the basis of the above-mentioned photocatalytic mechanism, the efficiency of the photocatalyst relates to the balance between charges separation, interfacial electron transfer and charge recombination. Generally speaking, the ease of the charge separation depends on a narrow band gap. The smaller E_g value is in favor of the electron transition, which may be beneficial to catalysis. So it is noted that the catalytic activities of complex **6** in agreement with the E_g values.
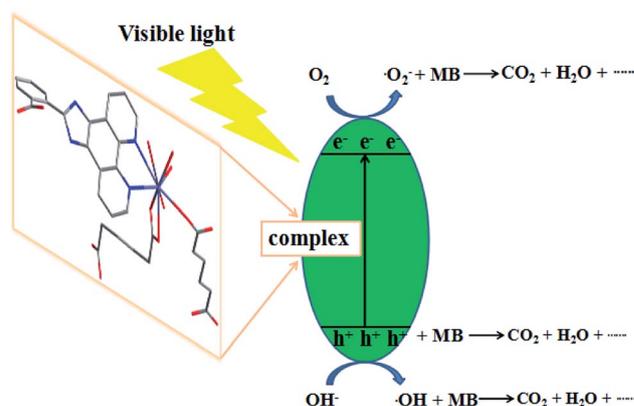

Fig. 21 Possible mechanism for the photo-induced charge transfer route of complex **6**.

Conclusions

In summary, we have hydrothermally synthesized six lanthanide(III) complexes by the reactions of 2-HNCP as the main ligand, and 3-HPYC, H$_2$SA and H$_2$AA as coligands, respectively. The structure analyses demonstrate that complexes **1**, **4**, **5** and **6** exhibit 2D layers, and complexes **2** and **3** display 1D chains. Finally, they all showed 3D supramolecular networks via C–H⋯π interactions or C–H⋯O inter-molecular hydrogen-bonding. TGA indicate that six complexes have remarkable thermal stabilities of the main framework. The PL spectra of these complexes exhibit the characteristic luminescence of the rare earth ion in the visible spectral regions at room temperature. Photocatalytic experiment results manifest that the complex **6** is more photocatalytically active for degrading MB dye under Xe lamp irradiation, which is an excellent potential candidate for photocatalytic degradation of organic pollutants. It is worth mentioning that the different coligands play important roles in the structures, thermal stabilities, photoluminescent properties and photocatalytic activities of same metal complexes. This work opens a new prospective and a feasible strategy for the application of complexes in photocatalytic degradation of organic pollutants by utilizing solar energy.

Conflicts of interest

There are no conflicts to declare.

Acknowledgements

Notes and references

1 J. Yu, L. H. Xie, J. R. Li, Y. Ma, J. M. Seminario and P. B. Balbuena, *Chem. Rev.*, 2017, **117**, 9674–9754.
2 V. J. Witherspoon, J. Xu and J. A. Reime, *Chem. Rev.*, 2018, **118**, 10033–10048.
3 C. Yao, W. Kang, S. R. Zhang, H. Y. Li, Y. H. Xu, Z. M. Su and G. B. Che, *RSC Adv.*, 2018, **8**, 36400–36406.
4 K. Sumida, D. L. Rogow, J. A. Mason, T. M. McDonald, E. D. Bloch, Z. R. Herm, T. H. Bae and J. R. Long, *Chem. Rev.*, 2012, **112**, 724–781.
5 M. D. Allendorf, C. A. Bauer, R. K. Bhakta and R. J. T. Houk, *Chem. Soc. Rev.*, 2009, **38**, 1330–1352.
6 M. Kurmoo, *Chem. Soc. Rev.*, 2009, **38**, 1353–1379.
7 B. Gole, A. K. Bara and P. S. Mukherjee, *Chem. Commun.*, 2011, **47**, 12137–12139.
8 L. Zhu, X. Q. Liu, H. L. Jiang and L. B. Sun, *Chem. Rev.*, 2017, **117**, 8129–8176.
9 C. C. Wang, J. R. Li, X. L. Lv, Y. Q. Zhang and G. S. Guo, *Energy Environ. Sci.*, 2014, **7**, 2831–2867.
10 M. Yoon, R. Srirambalaji and K. Kim, *Chem. Rev.*, 2011, **112**, 1196–1231.
11 S. Fukuzumi, Y. M. Lee and W. Nam, *Coord. Chem. Rev.*, 2018, **355**, 54–73.
12 W. Wang, M. O. Tadé and Z. Shao, *Prog. Mater. Sci.*, 2018, **92**, 33–63.
13 M. Sillanpää, M. C. Ncibi and A. Matilainen, *J. Environ. Manage.*, 2018, **208**, 56–76.
14 M. L. Aulsebrook, B. Graham, M. R. Grace and K. L. Tuck, *Coord. Chem. Rev.*, 2018, **395**, 191–220.
15 A. B. Ruiz-Muelle, A. García-García, A. A. García-Valdivia, I. Oyarzabal, J. Cepeda, J. M. Seco, E. Colacio, A. Rodríguez-Diéguez and I. Fernández, *Dalton Trans.*, 2018, **47**, 12783–12794.
16 J. Ma and B. Yan, *New J. Chem.*, 2018, **42**, 15061–15067.
17 N. Wang, J. W. Wang, D. Zhao, S. K. Mellerup, T. Peng, H. B. Wang and S. N. Wang, *Inorg. Chem.*, 2018, **57**, 10040–10049.
18 Q. S. Xia, X. D. Yu, H. M. Zhao, S. P. Wang, H. Wang, Z. F. Guo and H. Z. Xing, *Cryst. Growth Des.*, 2017, **17**, 4189–4195.
19 M. W. Drover, J. A. Love and L. L. Schafer, *Chem. Soc. Rev.*, 2017, **46**, 2913–2940.
20 D. Inci, R. Aydin, H. Huriyet, Y. Zorlu and N. Çinkılıç, *Appl. Organomet. Chem.*, 2018, **32**, e4309.
21 X. L. Wang, J. X. Zhang, G. C. Liu, H. Y. Lin and Z. H. Kang, *J. Coord. Chem.*, 2010, **63**, 3933–3943.
22 X. L. Wang, J. X. Zhang, G. C. Liu, H. Y. Lin and Y. Q. Chen, *Russ. J. Coord. Chem.*, 2010, **36**, 662–673.
23 Z. M. Li, Y. Qiao, C. B. Liu, Y. F. Zhou, X. Y. Wang, P. A. Charpentier, G. B. Che, W. Z. Xu, L. H. Liu and E. W. Zhu, *Dalton Trans.*, 2018, **47**, 7761–7775.
24 C. B. Liu, H. Y. Sun, X. Y. Li, H. Y. Bai, Y. Cong, A. Ren and G. B. Che, *Inorg. Chem. Commun.*, 2014, **47**, 80–83.
25 X. J. Zhang, W. K. Li, W. T. Zhang, G. B. Che, X. Y. Li, Y. Qiao and C. C. Zhao, *Inorg. Chem. Commun.*, 2015, **51**, 122–125.
26 Y. Qiao, Y. F. Zhou, W. S. Guan, L. H. Liu, B. Liu, G. B. Che, C. B. Liu, X. Lin and E. W. Zhu, *Inorg. Chim. Acta*, 2017, **466**, 291–297.
27 G. B. Che, S. Y. Liu, Q. Zhang, C. B. Liu and X. J. Zhang, *J. Solid State Chem.*, 2015, **225**, 378–382.
28 Y. Qiao, Z. M. Li, X. B. Wang, W. S. Guan, L. H. Liu, B. Liu, J. K. Wang, G. B. Che, C. B. Liu and X. Lin, *Inorg. Chim. Acta*, 2018, **471**, 397–403.
29 G. M. Sheldrick, *SHELXS-2014, Program for the Solution of Crystal Structures*, University of Göttingen, Germany, 2014.
30 G. M. Sheldrick, *SHELXL-2014, Program for the Refinement of Crystal Structure*, University of Göttingen, Germany, 2014.
31 X. L. Pang, L. Li, Y. Wei, X. D. Yu and Y. J. Li, *Dalton Trans.*, 2018, **47**, 11530–11538.
32 H. Y. Wong, W. T. K. Chan and G. L. Law, *Inorg. Chem.*, 2018, **57**, 6893–6902.
33 J. Z. Gu, Y. Cai, Y. Liu, X. X. Liang and A. M. Kirillov, *Inorg. Chim. Acta*, 2018, **469**, 98–104.

34 L. L. Luo, X. L. Qu, Z. Li, X. Li and H. L. Sun, *Dalton Trans.*, 2018, **47**, 925–934.

35 H. J. Zhang, R. Q. Fan, Y. W. Dong, W. Chen, X. Du, P. Wang and Y. L. Yang, *CrystEngComm*, 2016, **18**, 3711–3724.

36 B. Rajamouli and V. Sivakumar, *New J. Chem.*, 2017, **41**, 1017–1027.

37 S. H. Zottnick, W. G. Daul, C. Kerpen, M. Finze and K. Mueller-Buschbaum, *Chem.–Eur. J.*, 2018, **24**, 15287–15294.

38 W. T. Chen, Z. X. Zhang, H. Luo, Y. Sui and D. S. Liu, *Inorg. Chem.*, 2018, **57**, 11626–11632.

39 J. C. G. Bünzli, *Chem. Rev.*, 2010, **110**, 2729–2755.

40 Y. Qiao, S. S. Ren, L. H. Liu, W. S. Guan, Z. M. Li, G. B. Che, C. B. Liu, X. Y. Wang, Q. W. Wang and X. Y. Li, *J. Mol. Struct.*, 2018, **1161**, 238–245.

41 J. W. Cui, W. J. An, K. Van Hecke and G. H. Cui, *Dalton Trans.*, 2016, **45**, 17474–17484.

42 L. Zeng, X. Guo, C. He and C. Duan, *ACS Catal.*, 2016, **6**, 7935–7947.

43 H. N. Che, L. H. Liu, G. B. Che, H. J. Dong, C. B. Liu and C. M. Li, *Chem. Eng. J.*, 2019, **357**, 209–219.

44 H. N. Che, G. B. Che, E. H. Jiang, C. B. Liu, H. J. Dong and C. M. Li, *J. Taiwan Inst. Chem. Eng.*, 2018, **91**, 224–234.